nature materials

ARTICLES

https://doi.org/10.1038/s41563-019-0494-1

Directional massless Dirac fermions in a layered van der Waals material with one-dimensional long-range order

T. Y. Yang[1,12], Q. Wan[1,12], D. Y. Yan[2,3,12], Z. Zhu[4], Z. W. Wang[5], C. Peng[1], Y. B. Huang[6], R. Yu[5], J. Hu[7], Z. Q. Mao[8], Si Li[9], Shengyuan A. Yang[9], Hao Zheng[4,10], Jin -Feng Jia[4,10], Y. G. Shi[2,3,11] and N. Xu[1*]

One or a few layers of van der Waals (vdW) materials are promising for applications in nanoscale electronics. Established properties include high mobility in graphene, a large direct gap in monolayer MoS_2, the quantum spin Hall effect in monolayer WTe_2 and so on. These exciting properties arise from electron quantum confinement in the two-dimensional limit. Here, we use angle-resolved photoemission spectroscopy to reveal directional massless Dirac fermions due to one-dimensional confinement of carriers in the layered vdW material $NbSi_{0.45}Te_2$. The one-dimensional directional massless Dirac fermions are protected by non-symmorphic symmetry, and emerge from a stripe-like structural modulation with long-range translational symmetry only along the stripe direction as we show using scanning tunnelling microscopy. Our work not only provides a playground for investigating further the properties of directional massless Dirac fermions, but also introduces a unique component with one-dimensional long-range order for engineering nano-electronic devices based on heterostructures of vdW materials.

Layered van der Waals (vdW) materials have become one of the central topics in condensed-matter physics and materials science since the successful exfoliation of graphene[1]. Due to the quantum size effect of electrons in the two-dimensional (2D) limit, vdW materials with nanosized thickness display qualitative distinctions from bulk three-dimensional (3D) compounds, including the 2D massless Dirac fermion in graphene with extremely high mobility[1], the large and direct band gap in single-layered MoS_2 (ref. [2]), Ising superconductivity in MoS_2 and $NbSe_2$ (refs. [3,4]), the quantum spin Hall effect in monolayer WTe_2 (refs. [5–9]) and 2D ferromagnetism in single-layered CrI_3 (refs. [10,11]). Furthermore, due to the 2D crystal structural geometry, atomically thin layers of vdW materials can be assembled into heterostructures with high designability and manipulability, presenting emergent behaviours, for example superconductivity in the twisted bilayer graphene with magic angle[12,13]. The novel optical, electronic and mechanical properties in layered vdW materials and heterostructures hold great potential applications in the next generation of electronics and optoelectronics at the nanoscale.

Here, we present direct experimental evidence that $NbSi_{0.45}Te_2$, a vdW material with layered structure, exhibits one-dimensional (1D) confinement of its metallic surface state and yields directional massless Dirac fermions, as probed by angle-resolved photoemission spectroscopy (ARPES) measurements. The 1D behaviour originates from the remarkable stripe-like surface that only has long-range translation symmetry along the stripe direction as directly visualized by scanning tunnelling microscopy (STM) experiments. The non-symmorphic symmetry of the stripe structure guarantees the fourfold degeneracy of the Dirac node, and makes the directional massless Dirac fermions essential[14,15] and distinct from those relying on band inversion[16]. Our study not only experimentally reveals the directional massless Dirac fermions that are the 1D analogue to the 2D/3D ones in graphene/Dirac semimetals, but also provides a unique layered vdW monomer with 1D long-range order for constructing functional devices based on 2D heterostructures.

$NbSi_xTe_2$ is composed of stacked Te–($NbSi_x$)–Te sandwich layers, which can be considered as intercalation of Si into the 2H phase of transition metal dichalcogenide (TMD)(Fig. 1a). Distinct from other cases of the reaction of Fe (or Ni or Co) with (Nb,Ta)Te_2 (refs. [17–20]), which lead to a phase with structure unrelated to the parent compounds, $NbSi_xTe_2$ exhibits similar structural properties to the 2H-TMD with three different kinds of building units (Fig. 1b). In $NbSi_{1/3}Te_2$, as seen from Fig. 1c, the deformation induced by the intercalated Si atoms makes the original hexagonal structure of the $NbTe_2$ layer transform into a square plane[21]. $NbSi_{1/3}Te_2$ is effectively built from zigzag chains with (Nb–Nb)–(Si) cationic sequences (chains a and b in Fig. 1b) and the $NbTe_2$ chains (chain c in Fig. 1b), with abc chain succession (Fig. 1d). Si atoms adopt a Te square environment in the centre of the empty biprisms (Fig. 1e). The interlayer Te–Te distance is in the range of typical vdW type materials and atomically thin $NbSi_{1/3}Te_2$ flakes have been successfully fabricated by micro-exfoliation[22], which demonstrates the capability of $NbSi_{1/3}Te_2$ to be a component in nanoelectronics based on a vdW heterostructure. Topological semimetal phases are proposed in both bulk and single-layered $NbSi_{1/3}Te_2$ by first-principles calculations study[23]. As the Si intercalation level increases, more Nb atoms are paired and form the a(b) type chains. Because the Nb–Si bonding is necessary

[1]Institute for Advanced Studies, Wuhan University, Wuhan, China. [2]Beijing National Laboratory for Condensed Matter Physics and Institute of Physics, Chinese Academy of Sciences, Beijing, China. [3]School of Physical Sciences, University of Chinese Academy of Sciences, Beijing, China. [4]Key Laboratory of Artificial Structures and Quantum Control (Ministry of Education), Shenyang National Laboratory for Materials Science, School of Physics and Astronomy, Shanghai Jiao Tong University, Shanghai, China. [5]School of Physics and Technology, Wuhan University, Wuhan, China. [6]Shanghai Synchrotron Radiation Facility, Shanghai Institute of Applied Physics, Chinese Academy of Sciences, Shanghai, China. [7]Department of Physics, University of Arkansas, Fayetteville, AR, USA. [8]Department of Physics, Pennsylvania State University, University Park, PA, USA. [9]Research Laboratory for Quantum Materials, Singapore University of Technology and Design, Singapore, Singapore. [10]Tsung-Dao Lee Institute, Shanghai Jiao Tong University, Shanghai, China. [11]Songshan Lake Materials Laboratory, Dongguan, China. [12]These authors contributed equally: T. Y. Yang, Q. Wan, D. Y. Yan. *e-mail: nxu@whu.edu.cn

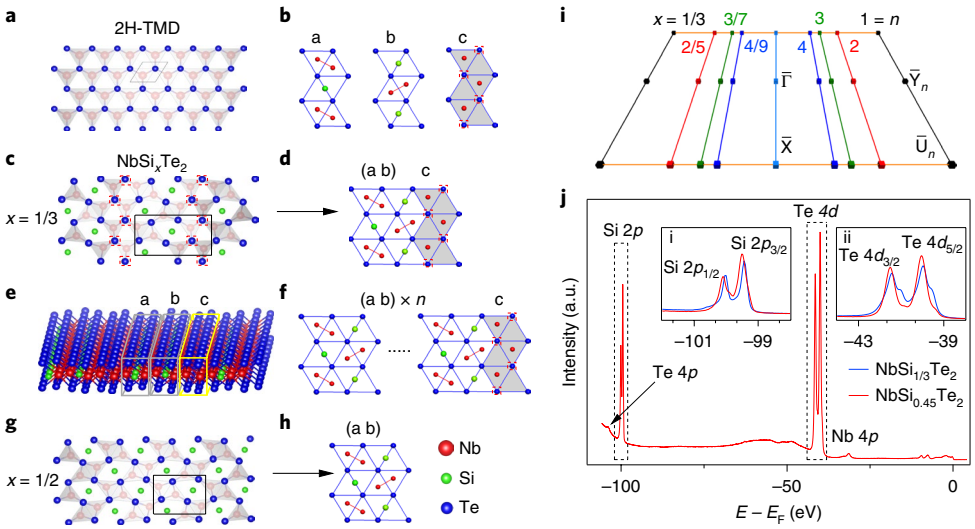

Fig. 1 | Crystal structure and core-level spectra of NbSi$_x$Te$_2$. **a**, Crystal structure of the 2H-TMD single layer. The light shadows indicate the coordination polyhedral. **b**, The schematic building units of NbSi$_x$Te$_2$. The red, green and blue balls represent the Nb, Si and Te atoms, respectively. The a/b units are zigzag chains with (Nb–Nb)–(Si) cationic sequences, and the c unit represents the NbTe$_2$ chains. The blue balls marked by red squares represent the Te atoms in c type chains with a different chemical environment from the others. **c**–**e**, Crystal structure (**c**), schematic (**d**) and 3D presentation (**e**) of the NbSi$_{1/3}$Te$_2$ single layer, which is composed of abc chain succession. **f**, The schematic of the NbSi$_x$Te$_2$ single layer, which is in a (ab)×*n*–c type structure. **g**,**h**, Crystal structure (**g**) and schematic (**h**) of the NbSi$_{1/2}$Te$_2$ single layer, which is composed of ab chain succession. **i**, Surface BZ of NbSi$_x$Te$_2$ with different *x* values. The corresponding *n* values for NbSi$_x$Te$_2$ with (ab)×*n*–**c** structure are also indicated. The light blue line in the centre represents the $\overline{\Gamma}$–$\overline{X}$ high-symmetry line. The black, red, green and blue lines correspond to $\overline{Y}_n$ – $\overline{U}_n$ high-symmetry lines for *n*=1, 2, 3 and 4, respectively. The orange lines represent the $\overline{X}$ – $\overline{U}_n$ high-symmetry line. The high-symmetry points $\overline{\Gamma}$, $\overline{X}$, $\overline{Y}_n$ and $\overline{U}_n$ are indicated by the dots with the same colours as the high-symmetry lines they are located on. **j**, Photoemission spectra in a wide energy range from the Fermi energy (E – E_F) for core levels of NbSi$_{0.45}$Te$_2$ (red lines) and NbSi$_{1/3}$Te$_2$ (blue lines). Insets i and ii are close ups of the Si 2*p* and Te 4*d* levels, respectively.

to stabilize the c type chains, two c chains are forbidden to be side by side[24]. Therefore, the NbSi$_x$Te$_2$ phase is composed of a (ab)×*n*–c type structure (Fig. 1f) with the relationship $x=n/(2n+1)$, where *n* is the number of (ab) blocks between adjacent c chains. The highest Si intercalation level is $x=1/2$ in NbSi$_{1/2}$Te$_2$ (Fig. 1g), which corresponds to the (ab) structure without any c chain (Fig. 1h). A longer periodicity along the *y* direction is expected for larger *x* value, for example ababc for $x=2/5$ and ababbabc for $x=3/7$. Correspondingly, the Brillouin zone (BZ) shrinks along the momentum (*k*) in the *y* direction, as illustrated by the (001) surface BZs for $x=1/3$, 2/5, 3/7 and 4/9 ($n=1$, 2, 3 and 4) shown in Fig. 1i.

The high-quality NbSi$_{0.45}$Te$_2$ single crystals used in this study were synthesized by the flux method (see Methods). The stoichiometry was determined by energy dispersive X-ray spectroscopy. In Fig. 1j, we present the photoemission intensity in a wide range of binding energy (E_B), in which Si 2*p* core-level peaks, together with those of the Nb 4*p* and Te 4*d* electrons, are clearly observed, confirming the successful intercalation of Si atoms in our single-crystal samples. The core-level data are compared with that obtained from NbSi$_{1/3}$Te$_2$, with the results shown in the insets of Fig. 1j. The Si 2*p* peaks for the $x=0.45$ sample (the red line in inset i of Fig. 1j) are more intensive than those of the $x=1/3$ sample (the blue line in inset i), indicating a higher Si intercalation level that is fully consistent with the energy dispersive X-ray spectroscopy results. For the Te 4*d* electrons, the shoulder-like features at lower E_B are strongly suppressed and the main peaks at higher E_B are enhanced in the $x=0.45$ sample, with the total area of Te 4*d* peaks unchanged. The shoulder-like features correspond to Te atom chains in the c chains that do not contain the intercalated Si atoms (indicated by the red dashed squares in Fig. 1b–d,f). Our core-level results (Fig. 1j) are fully consistent with the scenario shown in Fig. 1f, that the increase of Si intercalation level *x* reduces the ratio between the number of chain c to that of chain a (or b).

To verify the bulk/surface origin of the ARPES signals, we performed photon energy ($h\nu$, where h is Planck's constant and ν is the photon's frequency) -dependent measurements along the $\overline{\Gamma}$–$\overline{X}$ direction, with the constant energy plotted at the Fermi energy (E_F) (Fig. 2a). The most pronounced feature of the raw data shown in Fig. 2a is the sudden intensity suppression at $h\nu$ around 32 eV that corresponds to the antiresonance between the Nb 4*p* state to the valence state near E_F (Fig. 1j). Away from the antiresonance energy range, the photoemission intensity of the valence states recovers and then becomes weaker at higher $h\nu$ due to the smaller photoemission cross-section of Nb 4*d* electrons. Although the intensity is modulated with $h\nu$ in Fig. 2a, the momentum positions of the experimentally observed features show no variations with $h\nu$, suggesting a 2D Fermi surface (FS) configuration. To confirm the 2D nature of the observed valence bands near E_F, we plot the $h\nu$ dependence spectra taken at the $\overline{\Gamma}$ and $\overline{X}$ points of the surface BZ in Fig. 2b,c (indicated by cut1 and cut2 in Fig. 2a), with the corresponding energy distribution curves (EDCs) shown in Fig. 2d,e, respectively. The spectra taken with different $h\nu$ shown in Fig. 2b–e are normalized to total intensity, to eliminate intensity variation caused by the photoemission cross-section and to only focus on the band dispersions. Our results clearly indicate that there are no observable dispersions along the k_z direction for the experimentally determined electronic states at the $\overline{\Gamma}$ point, with one peak at $E_B\sim30$ meV and another broad peak at $E_B\sim300$ meV (Fig. 2b,d). Similarly, two non-dispersing bands are observed around 100 meV and 600 meV below E_F at the $\overline{X}$ point (Fig. 2c,e).

On the other hand, similar to the parent compound NbSe$_2$ (ref. [25]), TaSi$_{1/3}$Te$_2$ (ref. [26]) and the other vdW TMDs[27], electrons are expected to be coherently hopping between NbSi$_x$Te$_2$ layers, and form 3D FSs and a band structure that disperses along the k_z direction[23]. Therefore, the electronic state without k_z dispersion, as observed in our ARPES experiments here, corresponds to the

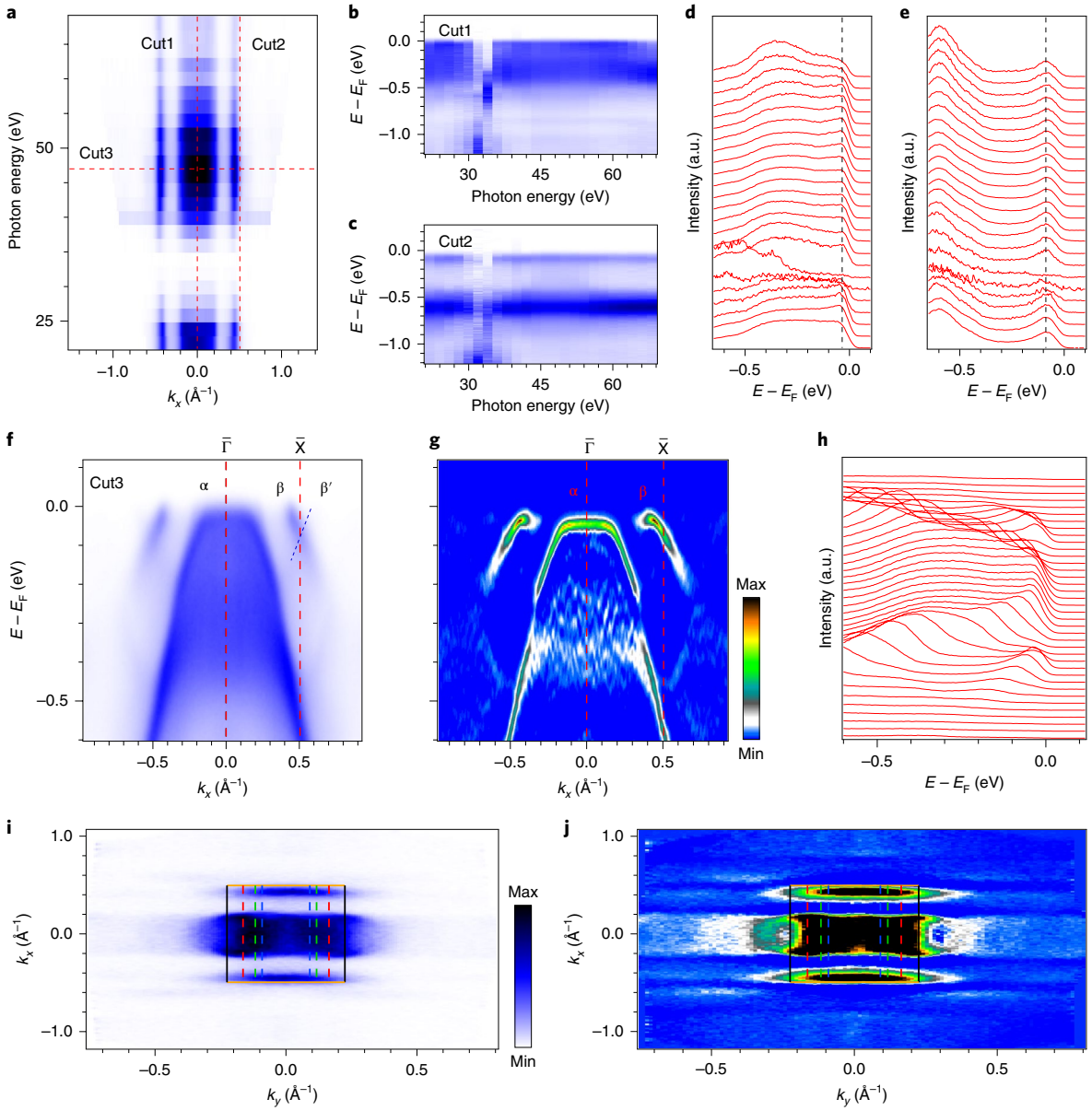

Fig. 2 | Surface electronic structure of $NbSi_{0.45}Te_2$. **a**, Plot of raw photoemission data at the Fermi energy (E_F) along the $\overline{\Gamma}$–$\overline{X}$ direction. **b**,**c**, Normalized photoemission intensity plots at the $\overline{\Gamma}$ and $\overline{X}$ points, as indicated by cut1 (**b**) and cut2 (**c**) in **a**. **d**,**e**, The corresponding EDC plots for cut1 (**d**) and cut2 (**e**). **f**–**h**, Photoemission intensity (**f**), curvature (**g**) and EDC (**h**) plots along the $\overline{\Gamma}$–$\overline{X}$ direction, indicated by cut3 in **a**. Bands near E_F are labelled as α and β. The dashed line in **f** indicates the β′ band, which is guaranteed by the translation symmetry along the *x* direction to be symmetric to the β band along the BZ boundary $\overline{X}$. The spectra weight of the β′ band is strongly suppressed along the $\overline{\Gamma}$–$\overline{X}$ high-symmetry line due to the photoemission selection rule. **i**,**j**, The photoemission intensity plot (**i**) and the corresponding curvature plot (**j**) at E_F in the k_x–k_y plane. The boxes indicate the surface BZs for the (ab)×*n*-c structures with several *n* values, as in Fig. 1i.

surface state, which originates from an uncommon stripe-like surface, as will be discussed below in greater detail.

We plot the surface band structure along the $\overline{\Gamma}$–$\overline{X}$ direction in Fig. 2f, probed by ARPES using photon energy $h\nu = 48$ eV, with the corresponding curvature and EDC plots shown in Fig. 2g,h, respectively. We observed a hole-like band, which we called α, with a relatively flat band top slightly below E_F near the $\overline{\Gamma}$ point (corresponding to the $E_B \sim 30$ meV peak shown in Fig. 2b,d). Another band, which we called β, shows an almost linear dispersion and crosses E_F near the surface boundary $\overline{X}$ point. Here we note that a band β' (indicated by the dashed line in Fig. 2f) is expected to appear and be symmetric to the β band along the BZ boundary $\overline{X}$, due to the translation symmetry along the *x* direction. The photoemission spectra weight of the β' band is strongly suppressed along the $\overline{\Gamma}$–$\overline{X}$ direction. This phenomenon, that photoemission from a certain band is observed in only every other BZ, was previously reported in non-symmorphic systems[27–30] because of a selection rule directly related to the non-primitive translation operations[28]. Here the absence of the β' band along the $\overline{\Gamma}$–$\overline{X}$ direction is induced by the non-symmorphic symmetry of the stripe region in $NbSi_{0.45}Te_2$. In fact, the same non-symmorphic symmetry protects the essential fourfold degeneracy point of the 1D Dirac dispersion observed near the stripe region in $NbSi_{0.45}Te_2$, together with the mirror and time reversal symmetry, which will be discussed later.

We map out the surface states in the k_x–k_y plane, with the FS intensity and the corresponding second derivative plotted in Fig. 2i,j,

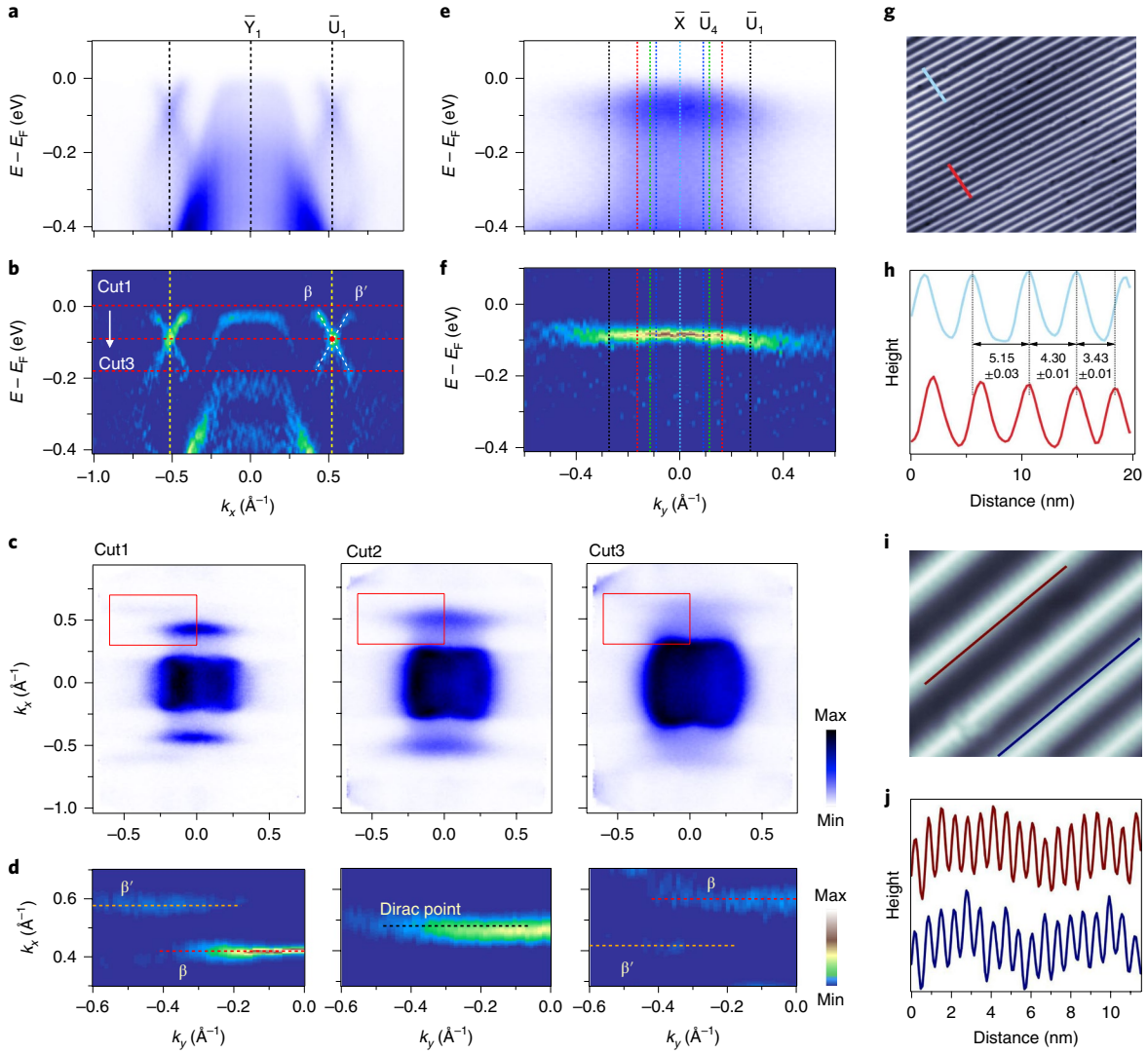

Fig. 3 | 1D Dirac dispersion on the stripe-like surface of $NbSi_{0.45}Te_2$. **a**,**b**, The photoemission intensity plot (**a**) and the corresponding curvature plot (**b**) along the $\bar{Y}_1$–$\bar{U}_1$ direction. **c**,**d**, The photoemission intensity plot (**c**) and the corresponding curvature plot (**d**) in an enlargedarea at different binding energies (E_B). The E_B of each panel is indicated by cut1–cut3 in **b**. The dashed lines are guides for the eye showing the β and β′ bands. **e**,**f** Same as **a**,**b**, but along the $\bar{X} - \bar{U}_n$ direction. The dashed lines indicate high-symmetry points $\bar{X}$ and $\bar{U}_n$, with the same colours as in Fig. 1i. **g**,**h**, A large-scale STM image (**g**, 100 × 100 nm^2, 400 mV, 1 nA) with two line profiles (**h**) clearly demonstrating the various values of interstripe distances (5.15 ± 0.03 nm, 4.30 ± 0.01 nm and 3.43 ± 0.01 nm). **i**,**j**, Atomic scale STM image (**i**, 14 × 14 nm^2, 300 mV, 0.5 nA) with two line profiles (**j**) showing the periodical lattice along the stripes with different interstripe distances.

respectively. The surface BZs for the (ab) × *n*–c structures with several *n* values are appended. Surprisingly, the observed FSs, especially the β (and the β') FS near the BZ boundary, show a clear 1D behaviour along the k_y direction within the whole region of surface BZs for various *n* values, which is very similar to the experimentally determined FS in the k_x–k_z plane (Fig. 2a). The combination of the out-of-plane and in-plane FS probed in our experiments (Fig. 2a,i) clearly demonstrates a 1D FS topology of the β band, which does not show dispersion along both the k_y and k_z directions.

Besides the 1D nature of the FS topology, the β band itself shows a 1D Dirac dispersion with an unusual Dirac point in the momentum space, as demonstrated by the results shown in Fig. 3. At the k_y value corresponding to the BZ boundary of $NbSi_{1/3}Te_2$ with $n = 1$ (the $\bar{Y}_1$–$\bar{U}_1$ direction in Fig. 1i), both the β band and the folding band β' can be clearly observed in the ARPES intensity plot (Fig. 3a) and the corresponding curvature plot (Fig. 3b), because the selection rule related to the non-symmorphic symmetry is not strictly applied off the $\bar{\Gamma}$–$\bar{X}$ direction. The β and β' bands cross each other along the k_x direction and form a Dirac dispersion, with the Dirac point with fourfold degeneracy around 0.1 eV below E_F. Such a Dirac dispersion displays a 1D behaviour, as indicated by the ARPES intensity in the surface BZ at several constant E_B shown in Fig. 3c and the corresponding curvature (Fig. 3d) in an enlarged region of Fig. 3c (marked by the red square). When the energy shifts from E_F to higher E_B (cut1 to cut3 in Fig. 3c,d), two straight lines (cut1), corresponding to the 1D β and β' FSs, firstly merge into a single line at $E_B \sim 0.1$ eV (cut2) and then separate into two lines again (cut3). The evolution of the β and β' bands is fully consistent with a 1D Dirac dispersion scenario. Figure 3e,f presents the ARPES intensity and curvature along the $\bar{X} - \bar{U}_n$ high-symmetry line, respectively, in that a single flat band is observed corresponding to the Dirac point. The results shown in Figs. 3e and 2c provide unambiguous experimental evidence of 1D Dirac dispersion hosted on the surface of $NbSi_{0.45}Te_2$; this Dirac point shows no dispersion along both the k_y

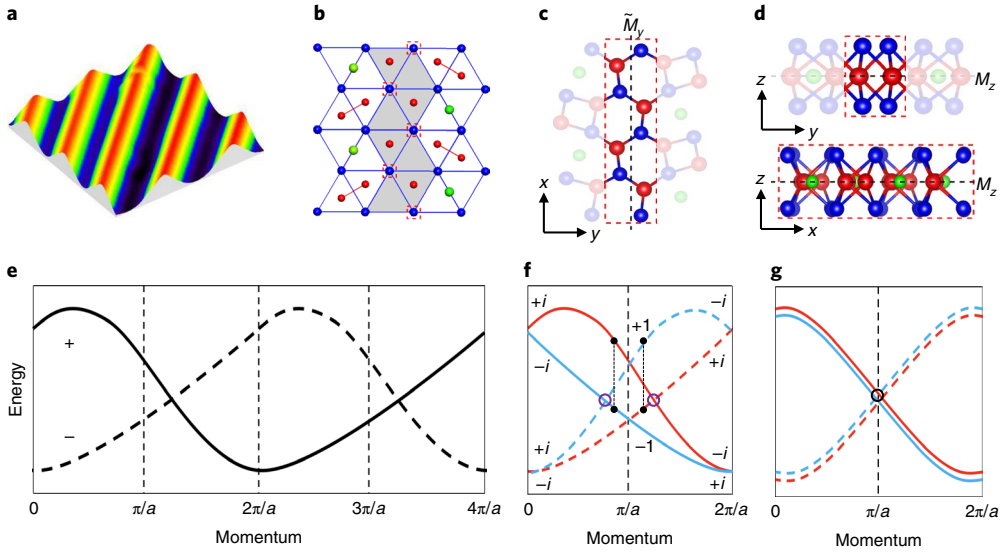

Fig. 4 | The non-symmorphic symmetry protected 1D Dirac dispersion with fourfold degeneracy. a, The three-dimensional presentation of STM results on the stripe surface of $NbSi_{0.45}Te_2$. **b**,**c**, The illustration (**b**) and crystal structure (**c**) near the c type chain in $NbSi_{0.45}Te_2$ projected along the *z* direction. The glide mirror ($\widetilde{M}_y$) is indicated by the black dashed line. **d**, The crystal structure of the c type chain region projected along the *x* and *y* directions. The mirror plane (M_z) is marked by the black dashed lines. The c type chain is highlighted by the shadow in **b** and the red dashed square in **c** and **d**. **e**, Band structure along the invariant line of glide mirror symmetry $\widetilde{M}_y$. The solid (dashed) line marked by + (−) indicates the main (folded) band. **f**, The combination of non-symmorphic and time reversal symmetries induces Weyl nodes on the invariant line. The red and blue solid (or dashed) lines indicate a pair of Kramers bands. The labels indicate the eigenvalues of $\widetilde{M}_y$. **g**, Together with mirror symmetry M_z, all bands are twofold degenerate and the essential Dirac point with fourfold degeneracy (marked by the black circle) occurs at π/a.

and k_z directions. We note that the α band shows a dispersive feature along the k_y direction in Fig. 3c. As discussed in the Supplementary Information (Supplementary Fig. 5), the observed dispersion periodicity of 1.5 $Å^{-1}$ relates well to the interblock spacing within the (ab)×*n* ribbons (b_0) of ~4.1 Å. It can be attributed to the intraribbon dispersion, similar to the intramolecule dispersion observed previously in sexiphenyl[31].

The unique 1D Dirac dispersion experimentally observed here is derived from an abnormal stripe-like structural modulation, which is directly visualized by STM experiments. As seen from Fig. 3g, stripes with alignment along the *x* direction are directly visualized on the $NbSi_{0.45}Te_2$ surface. This stripe-like pattern is a direct consequence of the c type chain component in the structure of $NbSi_xTe_2$ as shown in Fig. 1b. Because of the weak vdW interaction between the layers in $NbSi_xTe_2$, the surface probed by the STM experiment is terminated by Te atoms (Fig. 1e). The Te atoms in c type chains show a different chemical environment from the others due to the absence of Si intercalations in chain c (Fig. 1b–d,f). The different chemical environment can induce valence and height variations of Te atoms near the c type chain region, and results in the stripe-like contrast in the STM images (Fig. 3g). Interestingly, in a typical scale area of 100×100 nm^2, the distance between the stripes is not a constant, but varies from 3.43(±0.01) nm to 5.15(±0.03) nm (Fig. 3g,h). However, the lattice periodicity along the stripe direction remains a constant value of 6.35(±0.03) Å (Fig. 3i,j), which corresponds to the bulk lattice parameter *a* along the *x* direction. Therefore, our STM results on the $NbSi_{0.45}Te_2$ surface point to an unconventional stripe-like structural modulation where interstripe distances do not remain constant, whereas the long-range translational symmetry is preserved only along the stripe direction (the *x* axis).

Such an unusual stripe-like structural modulation with 1D long-range order is a unique property of the $NbSi_{0.45}Te_2$ system. As discussed above, the distance between the nearby bright stripes is the total width of the unit of (ab)×*n*–c, which is directly related to the Si stoichiometry *x* with the relationship $x=n/(2n+1)$. The interstripe distances of 3.43(±0.01) nm, 4.30(±0.01) nm and 5.15(±0.03) nm in Fig. 3g,h correspond to the (ab)×*n*–c units with $n=4$, 5 and 6, with the Si intercalation levels $x=4/9$, 5/11 and 6/13, respectively. The stoichiometry difference of Si between two successive *n* values is very tiny, that is 1% between $n=4$ and 5 stripes and 7‰ between $n=5$ and 6 stripes. In fact, the stoichiometry difference could be even smaller when both $n-1$ and $n+1$ stripes emerge together. In the case shown in Fig. 3g, the difference is 3‰ between a pair of stripes with $n=4,6$ and two stripes with $n=5$. Such tiny local stoichiometry fluctuations are hard, if not impossible, to avoid in the synthesizing process of complex compounds with more than 100 atoms in a (ab)×5–c unit ribbon. The fluctuations induce the unusual stripe-like structural modulation with 1D long-range order in $NbSi_{0.45}Te_2$, which in fact exhibits a type of atom arrangement[32] distinct from crystalline, quasicrystalline and amorphous.

The observation of the unique stripe structure with 1D long-range order provides a natural explanation of the 1D Dirac dispersion detected in our ARPES experiments. As indicated by the first-principles calculations in Supplementary Information (Supplementary Fig. 2), the Dirac dispersion formed by the β and β' bands is spatially localized around the c type chain regions that correspond to the stripes in the STM results. As the spacing blocks between stripes become more than two sets of (ab) chains, the interstripe hopping term can be ignored and the Dirac dispersion near E_F shows a quasi-1D behaviour. In $NbSi_{0.45}Te_2$, the stripe intervals vary from four to six sets of (ab) chains. Therefore, the 1D Dirac dispersion emerges on the surface of vdW material with 1D long-range order.

The fourfold degeneracy of the 1D Dirac dispersion observed in $NbSi_{0.45}Te_2$ is essential and protected by the non-symmorphic symmetry of the stripe region (Fig. 4a–c), together with the mirror (Fig. 4d) and time reversal symmetries. As shown in Fig. 4b,c, the crystal structure of the stripe region has a glide mirror symmetry $\widetilde{M}_y$ perpendicular to the *y* direction $\widetilde{M}_y(x,y,z) \rightarrow (x+1/2,-y,z)$. The $\widetilde{M}_y$ corresponds to a non-primitive translation operation along

the x direction, with eigenvalues of $g_{\widetilde{M}_y} = \pm\lambda e^{-ika/2}$, where a is lattice constant along the x direction. The additional phase term in $g_{\widetilde{M}_y}$ makes eigenstates in a 4π periodicity, that corresponds to two BZs. Figure 4e displays a generous case of band structure along the invariant line of $\widetilde{M}_y$, in that the dashed line is the folded band from the second BZ ($k-2\pi/a$), with an additional phase term ($e^{-i\pi}=-1$) in $g_{\widetilde{M}_y}$ compared to the main band. For $NbSi_{0.45}Te_2$, all the k points sit on the invariant line of $\widetilde{M}_y$ because of the 1D nature. Spin–orbit coupling has to be included, and therefore the coefficent (λ) takes a value of i and $g_{\widetilde{M}_y} = \pm ie^{-ika/2}$. Furthermore, time reversal symmetry T is reserved in $NbSi_{0.45}Te_2$, which induces Kramers pairs of the bands ($|u\rangle$ and $T|u\rangle$ indicated by the blue and red colours in Fig. 4f, respectively) degenerated at Kramers points ($k=0$ and π/a), for both the main and folded bands. Because of the commute relation between $\widetilde{M}_y$ and T,

$$\widetilde{M}_y T = T\widetilde{M}_y$$

values of $g_{\widetilde{M}_y}$ for Kramers pairs are complex conjugates of each other. Therefore, at Kramers points, the bands forming Kramers pairs have different values of $\widetilde{M}_y = \pm i$ at $k=0$ and the same values of $\widetilde{M}_y = 1$ (or -1) at $k=\pi$, as indicated in Fig. 4f. Finally, another mirror plane perpendicular to the z direction $M_z(x,y,z)\rightarrow(x,y,-z)$ is reserved in the structure of the stripe region (Fig. 4d). Similar to the case of $\widetilde{M}_y$, all the k points in $NbSi_{0.45}Te_2$ are invariant under the symmetry operation of M_z. Because $\widetilde{M}_y$ is anticommutative to M_z in the spin–orbit coupled $NbSi_{0.45}Te_2$,

$$\widetilde{M}_y M_z = -M_z\widetilde{M}_y$$

the degenerated eigenstates $|u\rangle$ and $M_z|u\rangle$ have opposite eigenvalues,

$$\widetilde{M}_y|u\rangle = g|u\rangle,$$

$$\widetilde{M}_y M_z|u\rangle = -M_z\widetilde{M}_y|u\rangle = -gM_z|u\rangle$$

In other words, each eigenstate $|u\rangle$ with $g_{\widetilde{M}_y} = g$ is degenerated with its partner $M_z|u\rangle$ with $g_{\widetilde{M}_y} = -g$, as shown in Fig. 4g. Consequently, a Dirac point with fourfold degeneracy appears at $k=\pi/a$ (Fig. 4g), which is guaranteed by the combination of $\widetilde{M}_y$, M_z and T.

The 1D Dirac dispersion with fourfold degeneracy observed in $NbSi_{0.45}Te_2$ is essential[14,15] and distinct from those created by band inversion[16,33–35]. The essential Dirac node is formed by a pair of bands with additional phase term ($e^{-i\pi}=-1$) in eigenvalues of the non-symmorphic symmetry operation ($\widetilde{M}_y$ in $NbSi_{0.45}Te_2$), and therefore band inversion is not indispensable to form the Dirac nodes. Due to the independence of band inversion, the only way to destroy the essential Dirac node is to lower the symmetries, so that the system can transit to either the topological or trivial insulator phase[14]. For the other distinct type of Dirac node observed in Na_3Bi/Cd_3As_2 (refs. [16,33–35]), a band inversion is necessary and a rotational symmetry guarantees the node with fourfold degeneracy. In this case, breaking the symmetry will open a gap at the Dirac nodes and induce a topological insulator phase. The trivial insulator phase is not adjacent to this kind of Dirac node related to band inversion in phase diagram. The non-symmorphic symmetry-protected Dirac nodal line[36,37] and Weyl node[38,39] have been observed in previous studies, which correspond to the 2D and 3D Dirac dispersions, respectively, and are distinct from the 1D case as seen in $NbSi_{0.45}Te_2$ (see Supplementary Fig. 3 in the Supplementary Information).

Our experiment thus points to a 1D confinement of the FS configuration on the surface of $NbSi_{0.45}Te_2$, induced by intercalation of Si atoms into the Nb–Si plane of TMD $NbTe_2$. They provide a direct demonstration of the realization of the 1D massless Dirac fermion. The 1D massless Dirac fermion observed in the present work, together with the 2D massless Dirac fermions in graphene[1] and topological nodal-line semimetal[36,40–42], and the 3D massless Dirac fermions in Na_3Bi/Cd_3As_2[16,33–35], form the complete group of massless Dirac fermions classfied with different dimensionalities. Our results indicate that the directional massless Dirac fermions are directly related to the unique stripes in $NbSi_{0.45}Te_2$ with 1D long-range order, and are protected by the non-symmorphic symmetry. Our experimental demonstration of 1D massless Dirac fermions not only opens a wealth of new opportunities for studying and controlling the 1D massless Dirac fermion, but also adds a unique component with 1D long-range order to the tool box of nanoelectronics based on vdW heterostructures.

Online content

Any methods, additional references, Nature Research reporting summaries, source data, statements of code and data availability and associated accession codes are available at https://doi.org/10.1038/s41563-019-0494-1.

Received: 25 February 2019; Accepted: 28 August 2019;
Published online: 7 October 2019

References

1. Novoselov, K. S. et al. Electric field effect in atomically thin carbon films. *Science* **306**, 666–669 (2004).
2. Mak, K. F., Lee, C., Hone, J., Shan, J. & Heinz, T. F. Atomically thin MoS_2: a new direct-gap semiconductor. *Phys. Rev. Lett.* **105**, 136805 (2010).
3. Lu, J. M. et al. Evidence for two-dimensional Ising superconductivity in gated MoS_2. *Science* **350**, 1353–1357 (2015).
4. Xi, X. X. et al. Ising pairing in superconducting $NbSe_2$ atomic layers. *Nat. Phys.* **12**, 139–143 (2016).
5. Qian, X. F., Liu, J. W., Fu, L. & Li, J. Quantum spin Hall effect in two-dimensional transition metal dichalcogenides. *Science* **346**, 1344–1347 (2014).
6. Fei, Z. Y. et al. Edge conduction in monolayer WTe_2. *Nat. Phys.* **13**, 677–682 (2017).
7. Tang, S. J. et al. Quantum spin hall state in monolayer 1T'-WTe_2. *Nat. Phys.* **13**, 683–687 (2017).
8. Wu, S. F. et al. Observation of the quantum spin hall effect up to 100 kelvin in a monolayer crystal. *Science* **359**, 76–79 (2018).
9. Zhu, Z. et al. Quasiparticle interference and nonsymmorphic effect on a floating band surface state of ZrSiSe. *Nat. Commum.* **9**, 4153 (2018).
10. Gong, C. et al. Discovery of intrinsic ferromagnetism in two-dimensional van der Waals crystals. *Nature* **546**, 265–269 (2017).
11. Huang, B. et al. Layer-dependent ferromagnetism in a van der Waals crystal down to the monolayer limit. *Nature* **546**, 270–273 (2017).
12. Cao, Y. et al. Unconventional superconductivity in magic-angle graphene superlattices. *Nature* **556**, 43–50 (2018).
13. Cao, Y. et al. Correlated insulator behaviour at half-filling in magic angle graphene superlattices. *Nature* **556**, 80–84 (2018).
14. Young, S. M. & Kane, C. L. Dirac semimetals in two dimensions. *Phys. Rev. Lett.* **115**, 126803 (2015).
15. Bzdušek, T., Wu, Q., Rüegg, A., Sigrist, M. & Soluyanov, A. A. Nodal-chain metals. *Nature* **538**, 75–78 (2016).
16. Wang, Z. et al. Dirac semimetal and topological phase transitions in $A3_Bi$ (A = Na, K, Rb). *Phys. Rev. B* **85**, 195320 (2012).
17. Li, J., Badding, M. E. & DiSalvo, F. J. New layered ternary niobium tellurides: synthesis, structure, and properties of niobium metal telluride. $NbMTe_2$ (M = iron, cobalt). *Inorg. Chem.* **31**, 1050–1054 (1992).
18. Huang, B., Shang, B. & Huang, J. Crystal structure of mixed metal cluster $Co_2Nb_2Te_4$ obtained by solid state reaction. *Jiegou Huaxue (J. Struct. Chem.)* **7**, 133 (1988).
19. Huang, B., Shang, B. & Huang, J. Crystal structure of mixed metal cluster $Ni_2Nb_2Te_4$ obtained by solid state reaction. *Jiegou Huaxue (J. Struct. Chem.)* **7**, 214 (1988).
20. Huang, B., Shang, B. & Huang, J. Synthesis and crystal structure of a new ternary tantalum chalcogenide $Ni_2Ta_2Te_4$. *Jiegou Huaxue (J. Struct. Chem.)* **8**, 145 (1989).
21. Li, J., Badding, M. E. & DiSalvo, F. J. Synthesis and structure of Nb_3SiTe_6, a new layered ternary niobium telluride compound. *J. Alloy. Compd.* **184**, 257–163 (1992).

22. Hu, J. et al. Enhanced electron coherence in atomically thin Nb_3SiTe_6. *Nat. Phys.* **11**, 471–476 (2015).
23. Li, Si et al. Nonsymmorphic-symmetry-protected hourglass dirac loop, nodal line, and dirac point in bulk and monolayer X_3SiTe_6 (X = Ta, Nb). *Phys. Rev. B* **97**, 045131 (2018).
24. Boucher, F., Zhukov, V. & Evain, M. MA_xTe_2 phases (M = Nb, Ta; A = Si, Ge; $1/3 \leq x \leq 1/2$): an electronic band structure calculation analysis. *Chem.* **35**, 7649–7654 (1996).
25. Weber, F. et al. Three-dimensional Fermi surface of 2H-$NbSe_2$: implications for the mechanism of charge density waves. *Phys. Rev. B* **97**, 235122 (2018).
26. Sato, T. et al. Observation of band crossings protected by nonsymmorphic symmetry in the layered ternary telluride Ta_3SiTe_6. *Phys. Rev. B* **98**, 121111(R) (2018).
27. Riley, J. M. et al. Direct observation of spin-polarized bulk bands in an inversion-symmetric semiconductor. *Nat. Phys.* **10**, 835–839 (2014).
28. Pescia, D., Law, A. R., Johnson, M. T. & Hughes, H. P. Determination of observable conduction band symmetry in angle-resolved electron spectroscopies: Non-symmorphic space groups. *Solid State Commun.* **56**, 809–812 (1985).
29. Finteis, Th et al. Occupied and unoccupied electronic band structure of WSe_2. *Phys. Rev. B* **55**, 10400 (1997).
30. Landolt, G. et al. Bulk and surface rashba splitting in single termination BiTeCl. *New J. Phys.* **15**, 085022 (2013).
31. Koller, G. et al. Intra- and intermolecular band dispersion in an organic crystal. *Science* **317**, 351–355 (2007).
32. Yin, D., Chen, C., Saito, M., Inoue, K. & Ikuhara, Y. Ceramic phases with one-dimensional long-range order. *Nat. Mater.* **18**, 19–23 (2019).
33. Liu, Z. K. et al. Discovery of a three-dimensional topological dirac semimetal, Na_3Bi. *Science* **343**, 864–867 (2014).
34. Neupane, M. et al. Observation of a three-dimensional topological dirac semimetal phase in high-mobility Cd_3As_2. *Nat. Commun.* **5**, 3786 (2014).
35. Borisenko, S. et al. Experimental realization of a three-dimensional dirac semimetal. *Phys. Rev. Lett.* **113**, 027603 (2014).
36. Schoop, L. M. et al. Dirac cone protected by non-symmorphic symmetry and three-dimensional dirac line node in ZrSiS. *Nat. Commun.* **7**, 11696 (2016).
37. Ekahana, S. A. et al. Observation of nodal line in non-symmorphic topological semimetal InBi. *New J. Phys.* **19**, 065007 (2017).
38. Schoop, L. M. et al. Tunable weyl and dirac states in the nonsymmorphic compound CeSbTe. *Sci. Adv.* **4**, eaar2317 (2018).
39. Nakayama, K. et al. Band splitting and weyl nodes in trigonal tellurium studied by angle-resolved photoemission spectroscopy and density functional theory. *Phys. Rev. B* **95**, 125204 (2017).
40. Weng, H. et al. Topological node-line semimetal in three-dimensional graphene networks. *Phys. Rev. B* **92**, 045108 (2015).
41. Bian, G. et al. Topological nodal-line fermions in spin-orbit metal $PbTaSe_2$. *Nat. Commun.* **7**, 10556 (2016).
42. Hu, J. et al. Evidence of topological nodal-line fermions in ZrSiSe and ZrSiTe. *Phys. Rev. Lett.* **117**, 016602 (2016).

Acknowledgements

This work was supported by the National Key R&D Programme of China (grant nos. 2018FYA0305800, 2016YFA0300403 and 2017YFA0302901), the Ministry of Science and Technology of China (grant no. 2018YFA0307000), the National Natural Science Foundation of China (grant nos. 11874047, 11674226, 11790313 and 11774399), the Fundamental Research Funds for the Central Universities (grant no. 2042018kf-0030), Beijing Natural Science Foundation (grant no. Z180008) and the K. C. Wong Education Foundation (grant no. GJTD-2018-01). Z.Q.M. acknowledges the support by the US Department of Energy under grant no. DE-SC0019068. N.X. acknowledges support by Wuhan University startup funding.

Author contributions

N.X. conceived the experiments. T.Y.Y, Q.W., C.P. and N.X. performed the ARPES measurements with the assistance of Y.B.H. D.Y.Y and Y.G.S. synthesized the $NbSi_{0.45}Te_2$ single crystals. Z.Z, H.Z. and J.-F.J. performed the STM measurements. Z.W.W, R.Y., S.L., S.A.Y. performed the ab initio calculations. J.H. and Z.Q.M synthesized the $NbSi_{1/3}Te_2$ single crystals as reference samples. T.Y.Y, Q.W., H.Z. and N.X. analysed the experimental data. N.X. wrote the manuscript. All authors discussed the results and commented on the manuscript.

Competing interests

The authors declare no competing interests.

Additional information

Supplementary information is available for this paper at https://doi.org/10.1038/s41563-019-0494-1.

Correspondence and requests for materials should be addressed to N.X.

Reprints and permissions information is available at www.nature.com/reprints.

Publisher's note Springer Nature remains neutral with regard to jurisdictional claims in published maps and institutional affiliations.

Methods

Sample synthesis. Single crystals of $NbSi_{0.45}Te_2$ were grown by using Te as flux. The starting materials Nb (powder, 99.99%, Alfa Aesar), Si (lump, 99.9999%, Alfa Aesar) and Te (lump, 99.999%, Alfa Aesar) were mixed in an Ar-filled glove box at a molar ratio of Nb:Si:Te = 3:1:30. The mixture was placed in an alumina crucible, which was then sealed in an evacuated quartz tube. The tube was heated to 1,100 °C over 10 h and then left for 20 h. Then, the tube was slowly cooled down to 800 °C at a rate of 2 °C h^{-1} and the crystals were then separated from the Te flux by centrifuging. Shiny crystals of size 2×2 mm^2 and of thickness of tens of micrometres were obtained on the bottom of the crucible.

ARPES. Clean surfaces for ARPES measurements were obtained by cleaving samples in situ in a vacuum greater than 5×10^{-11} Torr. Surface-sensitive vacuum-ultraviolet ARPES measurements were performed on the 'Dreamline' beamline of the Shanghai Synchrotron Radiation Facility (SSRF) with a Scienta Omicron DA30L analyser, with an overall energy resolution of the order of 20 meV at $T = 30$ K. The beam spot size in ARPES measurements is tens of microns.

STM. The STM measurements were conducted in a Unisoku STM (1600) at $T = 4.8$ K. The samples were cleaved in situ at room temperature under ultrahigh vacuum and then loaded into the STM head immediately. Electrochemically etched tungsten tips were used after in situ electron-beam cleaning and treated on a clean Ag(111) substrate.

Data availability

The data that support the plots within this paper and other findings of this study are available from the corresponding author upon reasonable request.